Experimental demonstration of a 5kW$_{th}$ granular-flow reactor for solar thermochemical energy storage with aluminum-doped calcium manganite particles

Andrew J. Schrader,[1] Garrett L. Schieber,[1] Andrea Ambrosini[2], and Peter G. Loutzenhiser[1*]
[1]George W. Woodruff School of Mechanical Engineering, Georgia Institute of Technology, Atlanta, Georgia USA, 30332-0405

[2] Concentrating Solar Technologies, Sandia National Laboratories, Albuquerque, NM 87185

[*]Corresponding Author: Peter G. Loutzenhiser, Email: peter.loutzenhiser@me.gatech.edu, Phone: +1. 404.894.3012

Abstract

A two-step cycle was considered for solar thermochemical energy storage based on aluminum-doped calcium manganite reduction/oxidation reactions for direct integration into Air Brayton cycles. The two steps encompassed 1) the storage of concentrated solar direct irradiation via the thermal reduction of aluminum-doped calcium manganite and 2) the delivery of heat to an Air-Brayton cycle via re-oxidation of oxygen-deficient aluminum-doped calcium manganite. The re-oxidized aluminum-doped calcium manganite was fed back to the first step to complete the cycle. A 5 kW$_{th}$ solar thermochemical reactor operating under vacuum was fabricated and tested to examine the first cycle reduction step. Reactor operating conditions and high-flux solar simulator control were tuned for continuous reactor operation with particle temperatures > 1073 K. Continuous operation was achieved using intermittent, dense granular flows. A maximum absorption efficiency of 64.7% was demonstrated, accounting for both sensible and chemical heat storage.

Keywords: *solar thermochemical reactor, dense granular flow, perovskite oxides, agglomeration, calcium manganites, thermochemical energy storage*

1. Introduction

Thermochemical energy storage (TCES) has been considered in two-step solar thermochemical cycles based on the reduction/oxidation (redox) of metal oxide particles for direct integration into an Air Brayton cycle to produce electricity [1-14].The direct irradiation of particles is ideal for achieving high temperature operation (> 1073 K) in solar thermochemical reactors [15]. The particles function simultaneously as both the heat transfer and TCES media, removing irreversible heat loss between different media [16]. This process requires novel solar receivers/reactors designed for the bulk transport behavior of granular media to direct irradiation of the TCES media. Granular media were observed to exhibit traits of solids (densely-packed particle structures), gases (dilute particle collisions), or liquids (dense particle flows) during bulk transport based on the relative impact of frictional and collisional effects [17-19]. Solid granular structures were achieved within solar receiver and solar thermochemical reactor designs with rotary kilns [20-22] and packed beds [23-26]. Dilute granular transport was achieved within solar receivers and solar thermochemical reactors using falling particle curtains [27-32], fluidized beds [33-35], and low-density flows along steep inclined planes [36-38]. Dense, granular flows have been achieved experimentally within solar receivers/reactors using slip-stick planes [39] gravity-fed tubes [40] and along inclined spirals [41, 42]. A 5 kW_{th} Solar Thermochemical Inclined Granular-Flow Reactor (STInGR) was designed, fabricated, modeled, and tested to characterize the reduction reaction of the directly-irradiated oxide particles using dense granular flows. TCES was modeled using directly-irradiated, thin (< 1mm) dense, granular flows of redox-active metal oxide particles [16, 41] via a combination of mass flow rate, slope inclination angles, and radiative conditions. Dense, granular flows are governed by the complex frictional and collisional interactions of particles, which are impacted by the presence of particle agglomeration at high temperatures.

A suite of experiments was performed in STInGR using spray-dried $CaAl_{0.2}Mn_{0.8}O_3$ (CAM28) granular powders to achieve continuous operation with bulk particle temperatures >1073 K. CAM28 crystallizes in the cubic perovskite structure and demonstrates continuous reduction over a wide range of temperature and O_2 partial pressure [7]. This makes it a promising candidate for high-temperature thermal storage, for example, coupled to an Air Brayton cycle. The average diameter of the CAM28 particles was $\overline{d}_p$ = 45 μm, determined from digital microscopy (Hirox

KH-3000 with ImagePro Plus image analysis software). The CAM28 was developed and optimized for two-step solar TCES cycles operating at ~1100 °C [7], represented as:

$$\mathrm{CaAl_{0.2}Mn_{0.8}O_{3-\delta}} + \frac{\delta}{2}\mathrm{O_2} \leftrightarrow \mathrm{CaAl_{0.2}Mn_{0.8}O_3} \tag{1}$$

where δ is the oxygen vacancy concentration (deviation from stoichiometry). Over the course of the experiments, particle agglomeration of the CAM28 occurred. Particle agglomeration has also been observed in chemical looping combustion reactors using spray-dried calcium manganite particles [43] and solar reactors and receivers with various energy storage materials [20, 36, 40, 44-48]. During agglomeration, individual particles retain their original shape, size, and properties but are held together by binding mechanisms, which include the formation of solid bridges from local sintering or chemical reactions between individual particles [49, 50]. The likelihood of agglomeration is amplified by the presence of fine particles [49]. The agglomeration results in deviations in granular flow behavior that must be addressed in the reactor design and/or operating conditions.

CAM28 agglomerate formation was investigated, and x-ray diffractometry (XRD) was employed to identify phase impurities contributing to agglomeration. The reactor design and operating conditions were optimized to overcome the agglomerate formation for continuous operation.

2. Experimental Setup

The STInGR system is schematically depicted in Figure 1 for (a) a Solidworks rendering of the reactor design and (b) a process flow diagram of the reactor with concentrated irradiation delivered by a high-flux solar simulator (HFSS) [51]. The cavity was fabricated using high-strength aluminosilicate boards (Zircar Zirconia M35 buster-type insulation). The boards were machined to form a 50 mm conical aperture with 45° acceptance angle, rectangular cavity ($150 \times 150 \times 100$ mm^3), a directly-irradiated slope, and a granular flow channel. Directly-irradiated cavity surfaces were coated with a reflective, high-purity alumina coating (Aremco PyroPaint AL). An 80 mm wide granular flow channel was produced from multiple, interlocking aluminosilicate boards to accommodate thermal expansion during high temperature operation. The boards were coated with high-purity alumina to develop a uniform surface roughness. The surface roughness was tuned to promote a dense granular flow at room temperature [16] and to reduce frictional wear of the aluminosilicate board [52]. The assembled granular flow channel resulted in a directly-irradiated stair-step granular flow path along the inclined plane to relieve thermal stresses during high temperature operation, shown in Figure 2.

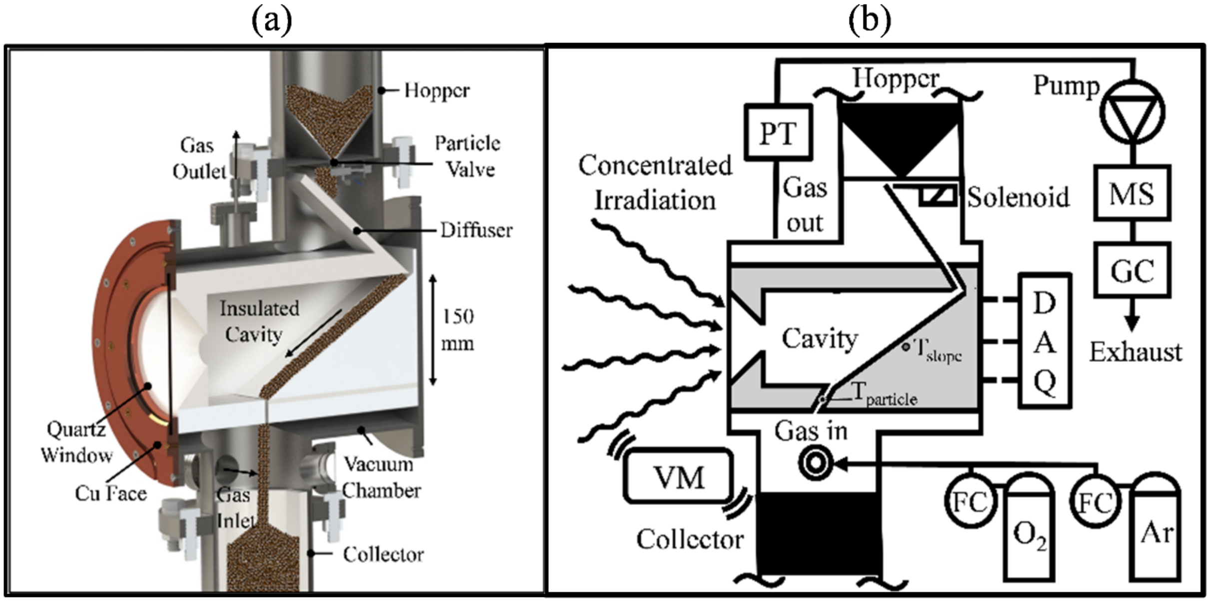

Figure 1. Design of the 5 kW_{th} solar thermochemical inclined granular-flow reactor with (a) a Solidworks rendering of the final design and (b) a process flow diagram of the reactor within the high-flux solar simulator

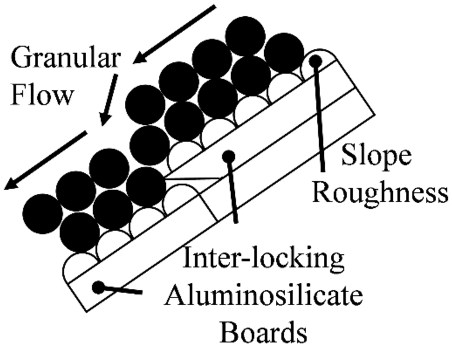

Figure 2. Schematic of granular flow channel composed of interlocking aluminosilicate boards to accommodate thermal expansion and producing a stair-step granular flow behavior

The reactor cavity was positioned in a stainless steel case (190 × 215 × 405 mm^3) within the vacuum chamber to ensure stability during high temperature operation. The vacuum chamber was fabricated from a stainless steel tube (NPS 10 Schedule 5) and fitted with steel flanges and feedthroughs for instrumentation during experimentation. The vacuum chamber was sealed with custom mica gaskets using a steel back plate, vertical cylindrical stainless steel hopper and collector assemblies (NPS 6 Schedule 5), and a water-cooled Cu face. A 5 mm thick, 140 mm diameter quartz window was housed within the water-cooled Cu face assembly and sealed using custom mica gaskets.

Concentrated irradiation from the HFSS was introduced through the quartz window, and reduced operating pressures were maintained with an oil-free rotary vane pump (Edwards nXDS10i oil-free scroll pump). The pressure was monitored with a transducer (PT, Omega PXM209) and convection gauge (Instrutech Series 101) during the experiments, ranging from 80 to 110 mbar. An Ar flow was introduced during experiments via mass flow controllers (FC, Bronkhorst F-201CV-20K-MAD-33-V) to maintain low O_2 partial pressures and high δ. Gas flows were introduced and removed via gas vacuum feedthroughs (Kurt J. Lesker F0275X4SWG). Gas compositions were temporally monitored using coupled gas chromatography (GC, Agilent 490 Micro GC with Molsieve and PoraPLOT Q columns) and mass spectrometry (MS, OmniStar ThermoStar GSD320 Gas Analysis System). Particles were loaded into an upper hopper assembly [53, 54] prior to experimentation. The mass flow rate was controlled with an orifice plate and solenoid valve [55, 56]. Particles were introduced into the granular flow channel using a diffuser plate, designed to reduce the particle kinetic energy and promote uniform flow depth and width. A dense, granular flow was achieved within a custom flow channel along the inclined plane and was directly irradiated by concentrated irradiation. A vibratory motor (VM, Vibco SPR-21) was attached to the structural frame to prevent agglomerate formation along the directly-irradiated flow channel during experimentation.

Sheathed, N-type thermocouples (Omega SNNXL-020U-8.5-SHX) were placed at two locations within the reactor cavity: 1) ~ 6–7 mm below the aluminosilicate board to measure cavity/granular flow channel temperature and 2) across the granular flow outlet to measure the average granular flow temperature. An array of N-type thermocouples was positioned at the flow outlet. The array was designed to be fully immersed in the exiting granular flow and shielded by an aluminosilicate overhang to prevent direct irradiation of the probes. Unsheathed, J-Type thermocouples (Omega 5TC-GG-J-20-6) were positioned within the reactor to measure lower temperature reactor cavity components and seals. Thermocouples penetrated the vacuum chamber via thermocouple vacuum feedthroughs (Kurt J. Lesker custom N-type XTEMP-FT and

TFT5JY00003). An infrared thermometer (ETEKCITY LaserGrip 1080 infrared thermometer) was used to determine the quartz window seal and the hopper surface temperature.

The fully fabricated STInGR is shown in Figure 3 for (a) the STInGR sealed with upper hopper and lower collector assemblies and mounted within the support frame, (b) the water-cooled Cu face, and (c) the assembled aluminosilicate cavity within the stainless steel sleeve.

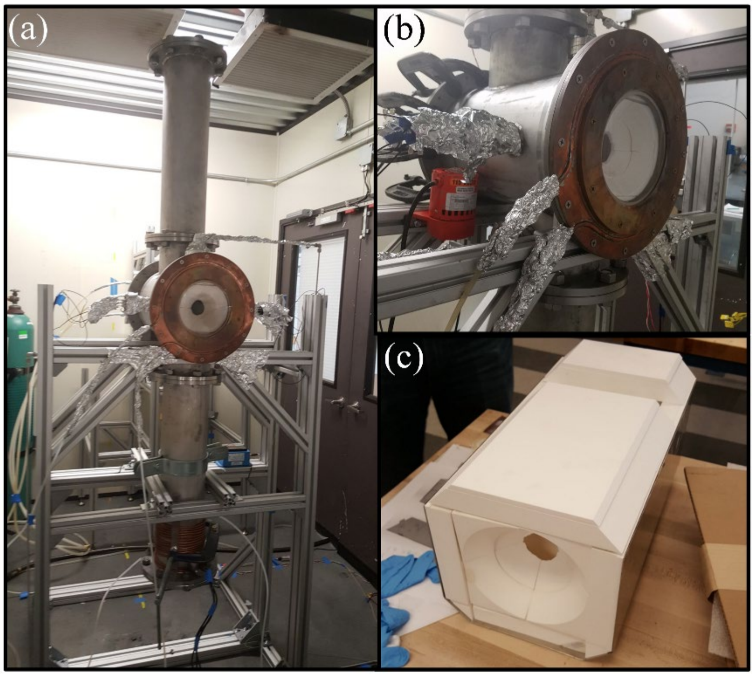

Figure 3. Fully-fabricated 5 kW_{th} solar thermochemical inclined granular flow reactor (a) front-view with upper hopper and lower collector assemblies mounted in the support frame, (b) closer, side-view, and (c) assembled aluminosilicate cavity within stainless steel sleeve.

3. Agglomeration of spray-dried calcium manganite particles

Preliminary experimentation was performed with dense, granular flows of spray-dried CAM28 for various slope inclination angles (θ_{slope}) and radiative inputs from the HFSS. Agglomerate formation was observed for sustained particle flow temperatures >1150 K at the flow outlet. The agglomerate structures are shown in Figure 4 (a) along the flow outlet bounded by the dashed line and (b) from an optical microscopy (Leica DVM 6 Optical Microscope) image taken after experimentation. The agglomerates formed along the inclined plane near the flow outlet, diverting flow around the structure and growing upwards along the flow channel over the course of the experiment. The agglomerate remained in place along the incline, as the gravitational shear was insufficient to overcome the inter-particle binding mechanisms. The optical microscopy image

(Figure 4b) showed signs of the formation of dendritic agglomeration [57, 58] , where the agglomerate was formed from weakly-bonded individual particles. The agglomerate did not adhere to the flow channel and was easily removed from the slope [36]; however, it retained a stable inter-particle agglomerate structure. Upon removal from the slope the agglomerates were found to break apart easily, returning to the original state with no appreciable change in particle size.

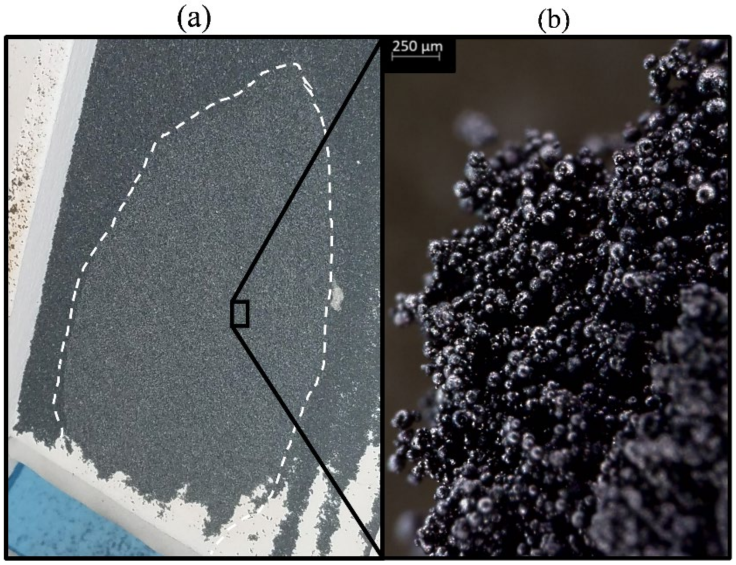

Figure 4. Agglomerate structures of spray-dried calcium manganite particles pictured (a) along the outlet of the granular flow channel bounded by the dashed line and (b) from an optical microscopy image of a structure removed from the reactor.

Powder X-ray diffraction (XRD, PANalytical X'Pert PRO Alpha-1 diffractometer with 2θ = 10 - 90°, step width 0.17°) was performed on the CAM28 particles and analyzed using MDI JADE 9 (Materials Data Inc. Jade+, Livermore, CA) powder diffraction analysis software and Powder Diffraction File 4+ reference database to identify phases present in the CAM28 formulation. XRD patterns are shown in Figure 5 for single-phase CAM28 synthesized as described in prior work [7], compared to spray-dried CAM28 particles in the as-received condition, cycled through multiple STInGR reduction/oxidation cycles, and additionally calcined in an air furnace (Sentro Tech Corp. ST-1600C-445) at 1473 K for 8 h. Single-phase CAM28 crystallizes in the cubic perovskite structure (PDF# 01-079-6765). The XRD patterns of the as-received spray-dried and STInGR-cycled particles revealed a secondary phase corresponding to the $CaMn_2O_4$ spinel structure (PDF# 4-015-3975). A related phase, Ca_2MnO_4, has been previously observed as an impurity in spray-dried calcium manganite particles, resulting in significant agglomeration for temperatures of 1173 to 1273 K [59]. Additional calcination of the spray-dried particles in air at 1473 K for 8 h, resulted in a decrease of the impurity spinel phase. As the Mn is in a lower oxidation state in $CaMn_2O_4$ than in the CAM28 (+3 and +4, respectively), it is thought that the additional calcination acts to oxidize the sample.

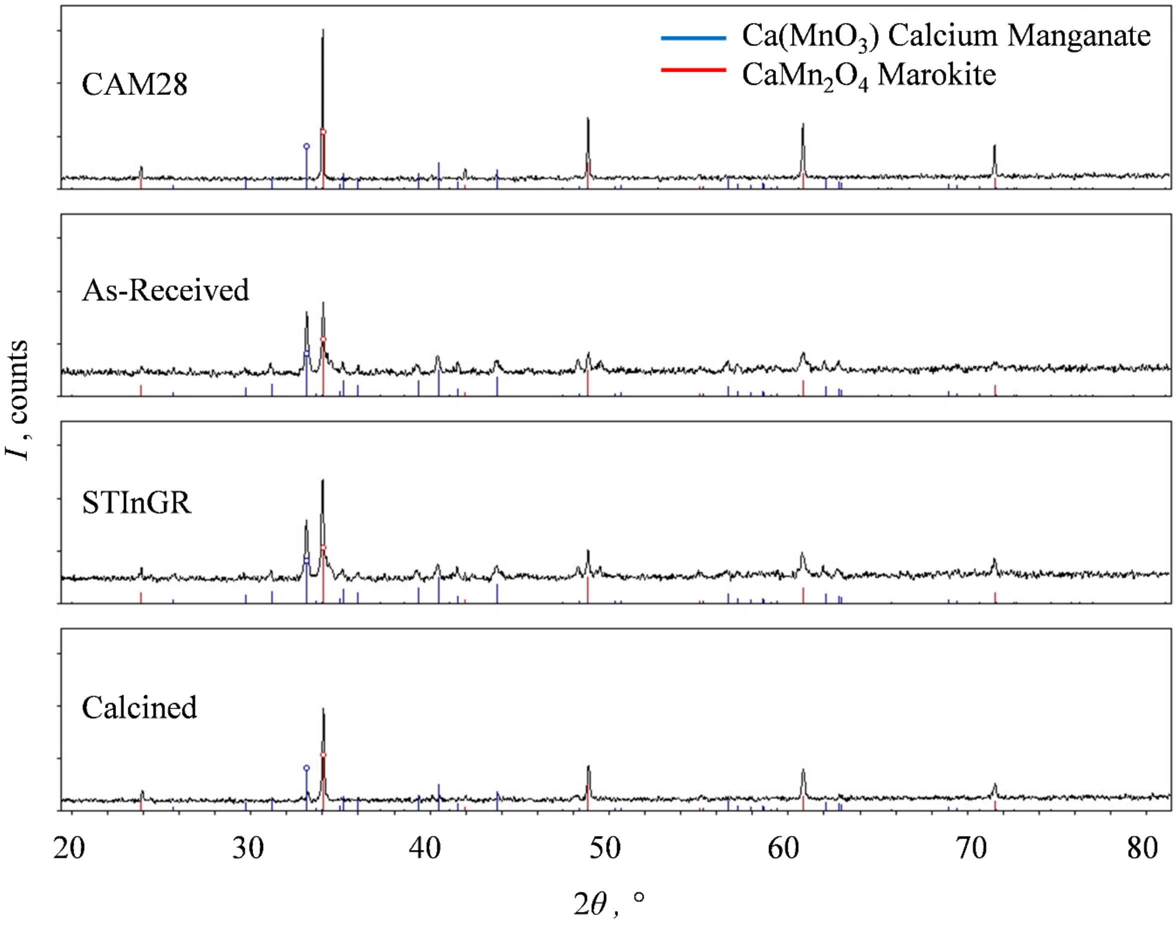

Figure 5. X-ray diffraction patterns of spray-dried, aluminum-doped calcium manganite granular powder samples in the as-received condition, cycled through multiple reactor (STInGR) reduction / oxidation cycles, and calcined in air at 1473 K for 8 hours. Single-phase $CaAl_{0.2}Mn_{0.8}O_{3-\delta}$ powder synthesized in the lab is shown for comparison. The peaks have been indexed to cubic perovskite $CaMnO_3$ (red) and $CaMn_2O_4$ spinel structure (blue).

4. Reactor Demonstration Results and Discussion

Experimental conditions were optimized for continuous flow that avoided agglomeration. STInGR performance was evaluated based upon the average outlet granular flow temperature, evolved O_2 (*i.e.*, calculated from the evolved O_2 flow), and absorption efficiency, given as:

$$\eta_{\text{abs}} = \frac{\dot{m}_{\text{flow}} \cdot \left(C_{\text{p}} \left[\overline{T}_{\text{particle}} - \overline{T}_{\text{hopper}} \right] + \Delta H_{\text{rxn},0\rightarrow\delta} \right)}{\dot{Q}_{\text{HFSS}}} \cdot 100 \tag{1}$$

where $\dot{m}_{\text{flow}}$ is the granular flow mass flow rate; C_{p} is the specific heat capacity of the aluminum-doped calcium manganite; T_{particle} is the outlet granular flow temperature; T_{hopper} is the hopper surface temperature; $\Delta H_{\text{rxn},0\rightarrow\delta}$ is the non-isothermal reduction enthalpy assuming stoichiometric deviation of $0 \rightarrow \delta$ based on evolved O_2 measurements of pure CAM28 [8, 60]; and $\dot{Q}_{\text{HFSS}}$ is concentrated radiative heat input delivered by HFSS lamps within the STInGR aperture at the focal plane. The specific heat of CAM28 was predicted with the Dulong-Petit law [7, 16, 61, 62] as 0.918 kJ/kg-K. This was accurately correlated to measured specific heats from differential scanning calorimetry (Netszch STA 409 C/CD) for pre-reduced CAM28 (1273 K) from 473 – 1273 K using the ASTM E 1269 standard. A comparison between measured and modeled specific heats is available in the Supplemental Material (Supplemental Fig. A). The experimental conditions during steady-state operation for two replicate experiments are given in Table 1. The cavity depth (l_{cavity}) and granular flow width (w) were optimized to avoid the formation of hot spots from individual lamps that resulted in agglomerates. θ_{slope} was selected to increase shear within the granular flow to inhibit agglomeration. T_{hopper} was measured at the completion of HFSS operation while particles continued to flow through the reactor cavity. The $\dot{m}_{\text{flow}}$ was determined from the total mass loss in the hopper and the total particle flow time. $\dot{Q}_{\text{HFSS}} = 4.43 \pm 0.03$ kW_{th} was determined from coupled calorimetry and flux map measurements at steady-state for the same lamp power inputs after the completion of the experiments. The five outer HFSS lamps delivered $\dot{Q}_{\text{HFSS}}$ to the reactor to reduce localized hot spots that lead to agglomerates. The spatial radiative fluxes were measured with a CCD camera for a Lambertian surface mounted in the focal plane. The pixel intensities were correlated to the spatial radiative heat fluxes [51, 63].

Table 1. Steady-state experimental conditions for reactor operation in the high-flux solar simulator

Parameters	Values
l_{cavity}	100 mm
w	80 mm
θ_{slope}	35°
Vibratory motor	On
$\dot{V}_{\text{Ar}}$	0.5 L_{N}/min

T_{hopper}	297 – 300 K
$\dot{m}_{\text{flow}}$	222 - 224 g/min
$\dot{Q}_{\text{HFSS}}$	4.43 ± 0.03 kW_{th}

The spatial radiative heat fluxes in the focal plane are given in Figure 6, with an overlaid 50 mm circle that denotes the STInGR aperture. Peak fluxes up to 3700 kW/m^2 were measured at the center of the aperture, and the fluxes decreased to between 1200 and 1600 kW/m^2 at the aperture edges. Higher radiative flux concentrations were measured at the lower portion of the aperture area, as the lower three lamps were operated at higher powers during experimentation.

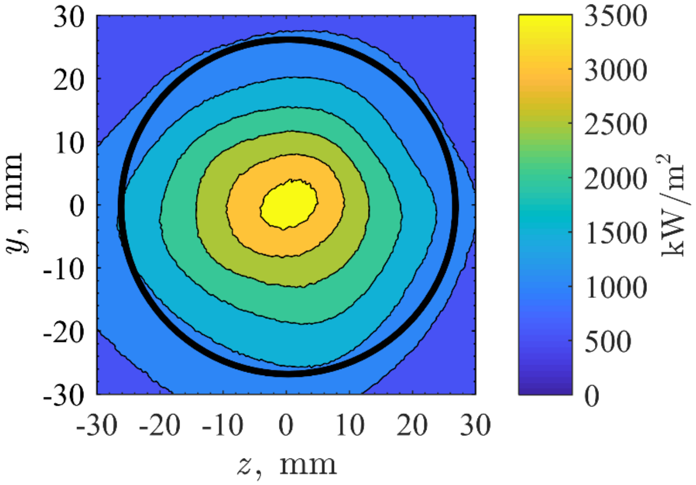

Figure 6. Measured radiative heat flux map in kW/m^2 at the focal plane of the high flux solar simulator, with the position of the reactor aperture represented by the black circle

4.1 *Intermittent, dense granular flows*

Agglomeration was avoided for the replicate experiments; however, increased inter-particle cohesion at high temperatures was observed. The increased cohesion produced intermittent, dense granular flows. Comparison between the desired, steady, granular flow [16, 19, 64] and the observed, intermittent granular flow during high-temperature operation is shown in Figure 7. The intermittent granular flow layer was thicker than expected compared to ambient temperatures, which resulted in direct exposure of the granular flow channel to concentrated irradiation during the experimental runs.

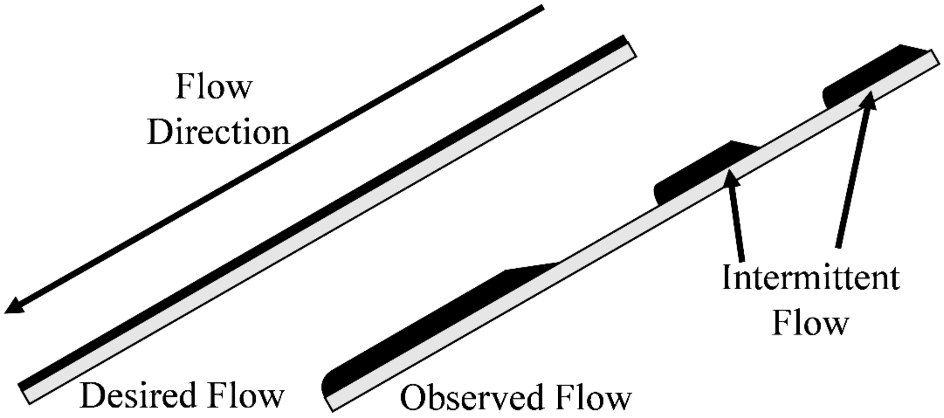

Figure 7. Schematic of desired, steady, dense granular flow compared to the observed, intermittent, dense granular flows during high temperature operation with the spray-dried, aluminum-doped calcium manganite granular powder

Two images of the intermittent, dense, granular flow viewed through the quartz window and aperture immediately following continuous reactor operation are displayed in Figure 8, normal to the aperture for (a) an initial frame and (b) a second frame 0.2 s later with the flow front indicated by a dashed line. The intermittent, dense granular flow was not evenly distributed across the flow channel as is shown by the non-uniform flow front and the exposed alumina within the flow. The intermittent flow was caused by a particle heap formed at the top of the incline as particles were introduced into the cavity. The heap formation was not observed at room temperature flow experiments [16], indicative of increased cohesion between particles at higher temperatures. The heap built-up until gravitational shear forces broke the heap and a dense, granular flow wave was developed along the incline. No particle agglomeration was observed along the incline. However, slight agglomeration was observed along the sidewalls near the particle outlet due to the increased frictional effects from the combined incline and sidewall interactions. When the HFSS was turned off, the slight agglomeration was dissipated by the continuous particle flow as the reactor cooled, indicating agglomeration formation was dependent on temperature. Hence, by adjusting parameters ting parameters such as mass flow rate, inclination angle, or concentrated irradiation levels minimize the formation of agglomerates.

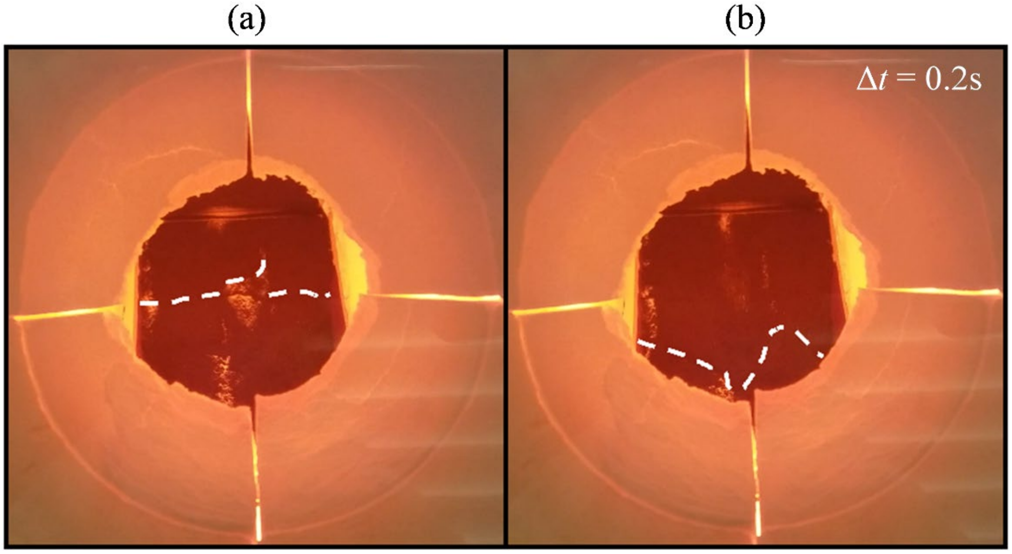

Figure 8. Images of intermittent, dense, granular flow of spray-dried aluminum-doped calcium manganite viewed through the quartz window and aperture immediately after high-flux solar simulator operation for (a) an initial frame and (b) a second frame 0.2 seconds later with the flow front indicated by a dashed line.

4.2 Continuous operation

Two experiments were performed under similar conditions to assess reactor performance. Prior to experimentation, the total pressure was reduced to < 80 mbar. For the continuous experiments, a steady pressure of 55-60 mbar was achieved using the vacuum pump. A 0.5 L_N/min (where L_N denotes liters at normal conditions of 273 K and 1 bar) flow of Ar was introduced to further reduce O_2 partial pressure (p_{O_2}). The experiment commenced with the introduction of concentrated irradiation. The temporal slope temperature (T_{slope}), average particle outlet temperature ($\overline{T}_{particle}$), evolved O_2 ($\dot{n}_{O_2}$), and $\dot{Q}_{HFSS}$ are shown in in Figure 9 for both replicated continuous experiments. The cavity was preheated for ~50 min using the three lower lamps until $T_{slope} \rightarrow 1073$ K. Once $T_{slope} = 1073$ K, particles were introduced to the cavity, and the VM was engaged to prevent agglomerate formation. $\dot{Q}_{HFSS}$ was increased after the particles were introduced by igniting two additional lamps and gradually increasing the power to the five lamps until near steady state was observed. The introduction of particles at $t = 70$ and 77 min resulted in a rapid decrease in T_{slope} and a rapid increase in $\overline{T}_{particle}$ and $\dot{n}_{O_2}$ as concentrated irradiation was stored sensibly and chemically in the flowing CAM28 particles. $\bar{T}_{\mathrm{particle}} > T_{\mathrm{slope}}$ was expected as the dense granular flow intercepted direct irradiation from the HFSS lamps and transferred the absorbed radiation downstream towards the outlet thermocouple array. The fluctuating measurements of $\bar{T}_{\mathrm{particle}}$ were due to intermittent granular flows striking the outlet thermocouple array. All the lamps were turned off after ~5 min of steady operation.

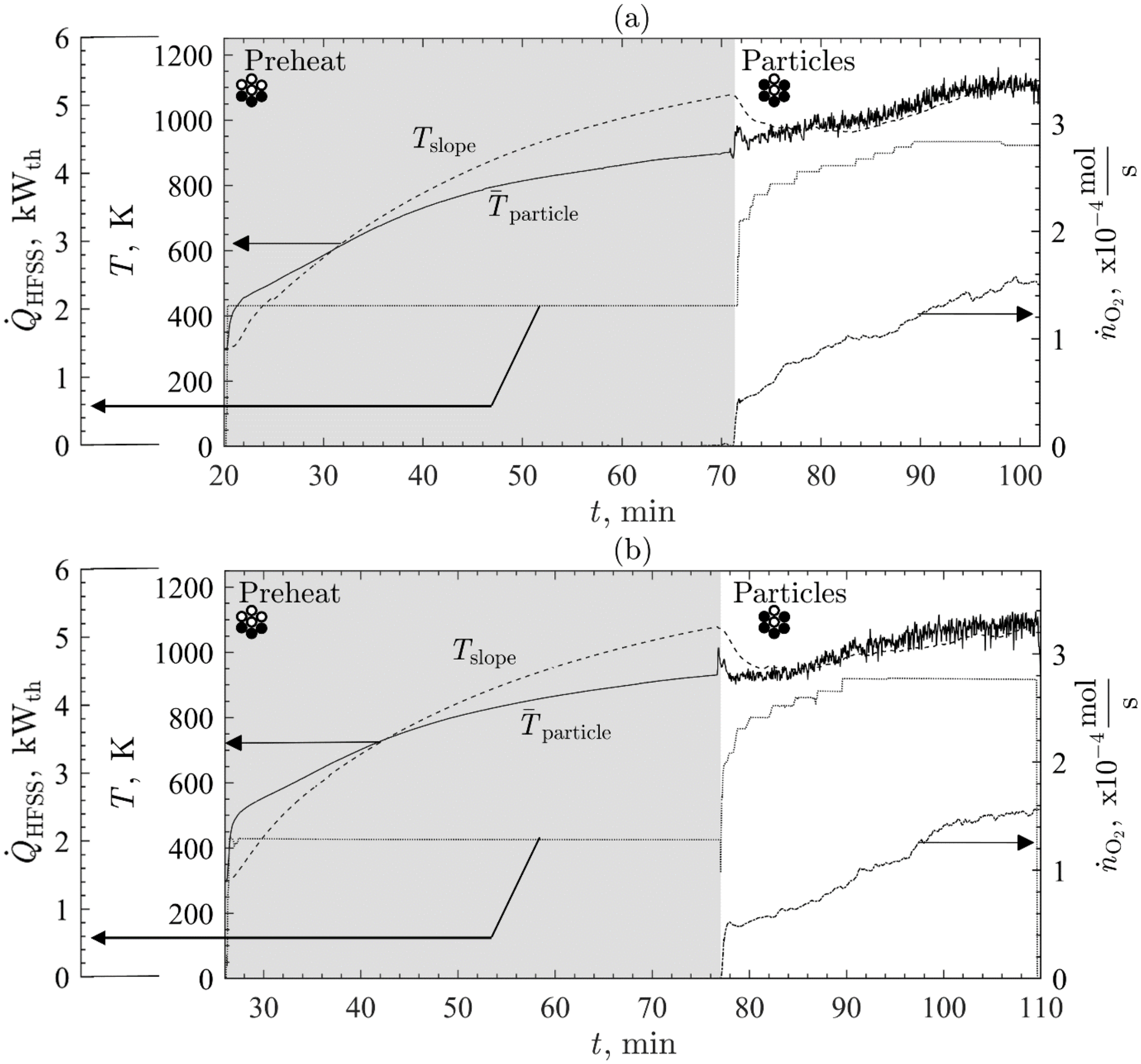

Figure 9. Experimental summaries of solar thermochemical inclined granular flow reactor experiments in the high-flux solar simulator including temporal measurements of outlet particle and slope (dash) temperatures, power delivered to a 50 mm aperture at the focal plane with representative lamp combinations (dotted), and evolved O_2 (dashed-dotted), for both preheat and particle flow operation regimes for (a) first and (b) second replicate experiments.

T_{particle}, T_{slope} and $\dot{n}_{O_2}$ are given as functions of time for steady-state operation in Figure 10 for two experiments approaching steady state. The range of T_{particle} between temporal max/min readings are indicated by the grayed region. Steady state was achieved for the final 2 min of operation for the second experiment (Figure 11b) as T_{slope} approached a steady isotherm. Rapid increases in T_{particle} were due to the intermittent, dense granular flow striking a portion of the thermocouple array. $T_{\text{particle}} > T_{\text{slope}}$ for particles in contact with the outlet thermocouple array. The wide range of T_{particle} when in contact with an intermittent flow was indicative of flow deviations across the granular flow width. The $\dot{n}_{O_2}$ remained constant during steady-state operation independent of the intermittent granular flow as dispersion through the reactor cavity dampened variations in the O_2 evolving from the granular flow.

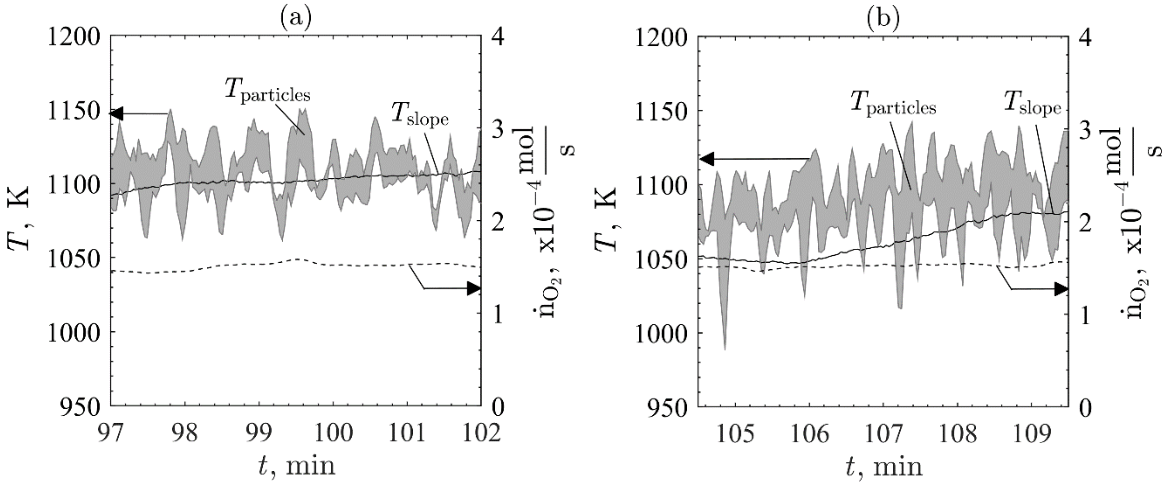

Figure 10. Temporal measurements of the temperature range of the slope temperature, particle temperature range (gray region), and evolved O_2 (dashed) for near steady-state operating conditions during high-flux solar simulator experimentation for (a) first and (b) second replicate experiments

The reactor performance metrics at steady-state are shown in Table 2 for $\overline{T}_{\text{particle}}$, $\Delta\delta$, and η_{total} for each experiment. A repeatable $\overline{T}_{\text{particle}}$ from 1112- 1123 K was measured during contact between the intermittent granular flow and the outlet thermocouple array. No agglomerates were formed along the directly irradiated flow channel. A bulk $\Delta\delta$ was between 0.0110 and0.0113 from both experiments, determined from evolved O_2 measurements. The low $\Delta\delta$ was due to a combination of reduced residence times of thin, granular flows along the directly irradiated portion of the flow channel and impurity phase(s) in the TCES material.

The impact of impurity phase(s) on reduction potential was investigated using thermogravimetric analysis (TGA, Netszch STA 449 F3 Jupiter) of granular powder samples with reduction cycles with 10% O_2/Ar flow at 1473 K and oxidation cycles with 80% O_2/Ar flow at 773 K. As-received, STInGR-cycled, and re-calcined granular powder samples all achieved a nearly identical mass loss/gain of 1.6%, which is significantly less than the 2.2% mass loss/gain predicted for single-phase CAM28 under similar cycling conditions. The smaller mass change is due to the presence of the spinel phase, which is not redox-active. A repeatable η_{abs} from 63.4% to 64.7% was achieved for STInGR experiments 1 and 2, respectively. Lower $\overline{T}_{\mathrm{particle}}$ and η_{total} were observed for the second experiment despite the reduced $\dot{m}_{\mathrm{flow}}$. This was likely due to a slightly lower $\dot{Q}_{\mathrm{HFSS}}$ in experiment 2. A low η_{abs} for both experiments was a result of the reflection losses from the quartz window, the water-cooled Cu plate, and the restricted flow width.

Table 2. Average and standard deviation of steady-state reactor performance parameters measured during replicate experiments

Experiment	1	2
$\overline{T}_{\mathrm{particle}}$	1123 ± 21 K	1112 ± 22 K
$\Delta\delta$	0.0110 ± 0.0002	0.0113 ± 0.0002
η_{abs}, %	64.7 ± 1.7%	63.4 ± 1.8 %

4. Summary and Conclusions

The 5 kWth solar thermochemical inclined granular-flow reactor was tested in a high flux solar simulator using spray-dried aluminum-doped calcium manganite particles as a heat transfer and thermochemical energy storage medium. The reactor was designed to efficiently store concentrated solar irradiation sensibly and chemically in dense, granular flows of particles for continuous on-sun operation. Particle agglomeration was investigated, and x-ray diffractometry was used to identify potential impurity phases that promoted agglomeration and decreased thermal reduction performance. The reactor and high-flux solar simulator operating conditions were tuned to mitigate severe inter-particle agglomeration observed in the spray-dried aluminum-doped calcium manganite particles for temperatures exceeding 1150 K. The reactor was operated continuously using dense granular flows of particles with bulk granular flow temperatures greater than 1073 K, thermochemical energy storage, and a maximum absorption efficiency of 64.7%.

The results from the experimental campaign provide valuable insights into the performance of granular flow reactors that operate continuously. While inter-particle agglomeration introduced a significant challenge, the initial experimental results showed that the operating conditions are tunable for overcoming agglomeration formations.

Acknowledgements

This material is based upon work supported by the U.S. Department of Energy's Office of Energy Efficiency and Renewable Energy under the Sunshot Initiative Award Number DE-EE-0000805. Sandia National Laboratories is a multimission laboratory managed and operated by National Technology & Engineering Solutions of Sandia, LLC, a wholly owned subsidiary of Honeywell International Inc., for the U.S. Department of Energy's National Nuclear Security Administration under contract DE-NA0003525. This paper describes objective technical results and analysis. Any subjective views or opinions that might be expressed in the paper do not necessarily represent the views of the U.S. Department of Energy or the United States Government. The authors wish to thank Drs. Sean Babiniec and Eric Coker from Sandia National Laboratories for assistance with synthesis and thermophysical characterization of the calcium manganite particles.

Nomenclature

C_p	specific heat
d	diameter
ΔH	enthalpy
l	length
m	mass
n	moles
P	pressure
Q	thermal energy
T	temperature
V	volume
w	flow width

Greek Letters

δ	non-stoichiometric oxygen vacancy concentration
Δ	change in property
η	efficiency
θ	angle

Subscripts

abs	absorption
cavity	reactor cavity
flow	particle flow
O_2	oxygen gas
Ar	argon gas
particle	particles
hopper	hopper surface
rxn	reaction
slope	inclined slope

Superscripts/Accents

$\dot{}$	time rate of change
$\bar{}$	average

Abbreviations

CAM28	$CaAl_{0.2}Mn_{0.8}O_{3-\delta}$
DAQ	data acquisition
GC	gas chromatograph
HFSS	high-flux solar simulator
MS	mass spectrometer
PT	pressure transducer
STInGR	Solar Thermochemical Inclined Granular Flow Reactor
VM	vibratory motor

XRD	x-ray diffractometry

References:

[1] S. Wu, C. Zhou, E. Doroodchi, R. Nellore, B. Moghtaderi, A review on high-temperature thermochemical energy storage based on metal oxides redox cycle, Energy Conversion and Management, 168 (2018) 421-453.

[2] A.J. Schrader, A.P. Muroyama, P.G. Loutzenhiser, Solar electricity via an Air Brayton cycle with an integrated two-step thermochemical cycle for heat storage based on Co_3O_4/CoO redox reactions: Thermodynamic analysis, Sol. Energy, 118 (2015) 485-495.

[3] C. Pagkoura, G. Karagiannakis, A. Zygogianni, S. Lorentzou, M. Kostoglou, A.G. Konstandopoulos, M. Rattenburry, J.W. Woodhead, Cobalt oxide based structured bodies as redox thermochemical heat storage medium for future CSP plants, Sol. Energy, 108 (2014) 146-163.

[4] A.J. Carrillo, J. González-Aguilar, M. Romero, J.M. Coronado, Solar energy on demand: A review on high temperature thermochemical heat storage systems and materials, Chemical reviews, 119 (2019) 4777-4816.

[5] H.E. Bush, P.G. Loutzenhiser, Solar electricity via an Air Brayton cycle with an integrated two-step thermochemical cycle for heat storage based on Fe_2O_3/Fe_3O_4 redox reactions: Thermodynamic and kinetic analyses, Solar Energy, 174 (2018) 617-627.

[6] B. Wong, Thermochemical Heat Storage for Concentrated Solar Power, Final Report for the US Department of Energy, in, San Diego, CA, USA, 2011.

[7] S.M. Babiniec, E.N. Coker, J.E. Miller, A. Ambrosini, Doped calcium manganites for advanced high-temperature thermochemical energy storage, International Journal of Energy Research, 40 (2016) 280-284.

[8] S.M. Babiniec, E.N. Coker, J.E. Miller, A. Ambrosini, Investigation of $La_xSr_{1-x}Co_yM_{1-y}O_{3-\delta}$ (M = Mn, Fe) perovskite materials as thermochemical energy storage media, Solar Energy, 118 (2015) 451-459.

[9] L. Imponenti, K.J. Albrecht, R. Kharait, M.D. Sanders, G.S. Jackson, Redox cycles with doped calcium manganites for thermochemical energy storage to 1000° C, Applied Energy, 230 (2018) 1-18.

[10] B.T. Gorman, N.G. Johnson, J.E. Miller, E.B. Stechel, Thermodynamic Investigation of Concentrating Solar Power With Thermochemical Storage, in, 2015.

[11] A. Bayon, R. Bader, M. Jafarian, L. Fedunik-Hofman, Y. Sun, J. Hinkley, S. Miller, W. Lipiński, Techno-economic assessment of solid–gas thermochemical energy storage systems for solar thermal power applications, Energy, 149 (2018) 473-484.

[12] Q. Lei, R. Bader, P. Kreider, K. Lovegrove, W. Lipiński, Thermodynamic analysis of a combined-cycle solar thermal power plant with manganese oxide-based thermochemical energy storage, in: E3S Web of Conferences, Vol. 22, EDP Sciences, 2017, pp. 00102.

[13] Y. Criado, M. Alonso, J. Abanades, Z. Anxionnaz-Minvielle, Conceptual process design of a CaO/Ca(OH)$_2$ thermochemical energy storage system using fluidized bed reactors, Applied Thermal Engineering, 73 (2014) 1087-1094.

[14] X. Zhou, M. Mahmood, J. Chen, T. Yang, G. Xiao, M.L. Ferrari, Validated model of thermochemical energy storage based on cobalt oxides, Applied Thermal Engineering, 159 (2019) 113965.

[15] A. Steinfeld, Solar thermochemical production of hydrogen—a review, Sol. Energy, 78 (2005) 603-615.

[16] A.J. Schrader, H.E. Bush, D. Ranjan, P.G. Loutzenhiser, Aluminum-doped calcium manganite particles for solar thermochemical energy storage: Reactor design, particle characterization, and heat and mass transfer modeling, International Journal of Heat and Mass Transfer, 152 (2020) 119461.

[17] B. Andreotti, Y. Forterre, O. Pouliquen, Granular media: between fluid and solid, Cambridge University Press, 2013.

[18] Y. Forterre, O. Pouliquen, Flows of dense granular media, Annu. Rev. Fluid Mech., 40 (2008) 1-24.

[19] G. MiDi, On dense granular flows, Eur. Phys. J., 14 (2004) 341-365.

[20] M. Neises, S. Tescari, L. de Oliveira, M. Roeb, C. Sattler, B. Wong, Solar-heated rotary kiln for thermochemical energy storage, Sol. Energy, 86 (2012) 3040-3048.

[21] R. Muller, P. Haeberling, R.D. Palumbo, Further advances toward the development of a direct heating solar thermal chemical reactor for the thermal dissociation of ZnO(s), Sol. Energy, 80 (2005) 500-511.

[22] L.O. Schunk, P. Haeberling, S. Wepf, D. Wuillemin, A. Meier, A. Steinfeld, A Receiver - Reactor for the Solar Thermal Dissociation of Zinc Oxide, J. Sol. Energ. Eng., 130 (2008).

[23] D.W. Gregg, W.R. Aiman, H.H. Otsuki, C.B. Thorsness, Solar coal gasification, Solar Energy, 24 (1980) 313-321.

[24] R.W. Taylor, R. Berjoan, J.P. Coutures, Solar gasification of carbonaceous materials, Solar Energy, 30 (1983) 513-525.

[25] S. Bellan, E. Alonso, F. Gomez-Garcia, C. Perez-Rabago, J. Gonzalez-Aguilar, M. Romero, Thermal performance of lab-scale solar reactor designed for kinetics analysis at high radiation fluxes, Chem. Eng. Sci., 101 (2013) 81-89.

[26] I. Ermanoski, N.P. Siegel, E.B. Stechel, A New Reactor Concept for Efficient Solar-Thermochemical Fuel Production, J. Sol. Energy Eng., 135 (2013).

[27] C. Ho, J. Christian, D. Gill, A. Moya, S. Jeter, S. Abdel-Khalik, D. Sadowski, N. Siegel, H. Al-Ansary, L. Amsbeck, Technology advancements for next generation falling particle receivers, Energy Procedia, 49 (2014) 398-407.

[28] C.K. Ho, J.M. Christian, J. Yellowhair, K. Armijo, W.J. Kolb, S. Jeter, M. Golob, C. Nguyen, Performance evaluation of a high-temperature falling particle receiver, in: ASME 2016 10th International Conference on Energy Sustainability collocated with the ASME 2016 Power Conference and the ASME 2016 14th International Conference on Fuel Cell

Science, Engineering and Technology, American Society of Mechanical Engineers, 2016, pp. V001T004A006-V001T004A006.

[29] C.K. Ho, J.M. Christian, J. Yellowhair, N. Siegel, S. Jeter, M. Golob, S.I. Abdel-Khalik, C. Nguyen, H. Al-Ansary, On-sun testing of an advanced falling particle receiver system, in: AIP Conference Proceedings, Vol. 1734, AIP Publishing, 2016, pp. 030022.

[30] N. Siegel, G. Kolb, Design and on-sun testing of a solid particle receiver prototype, in: 2008 2nd International Conference on Energy Sustainability, ES 2008, August 10, 2008 - August 14, 2008, Vol. 2, ASME, Jacksonville, FL, United states, 2009, pp. 329-334.

[31] N.P. Siegel, C.K. Ho, S.S. Khalsa, G.J. Kolb, Development and evaluation of a prototype solid particle receiver: on-sun testing and model validation, Journal of Solar Energy Engineering, 132 (2010) 021008.

[32] C.K. Ho, A review of high-temperature particle receivers for concentrating solar power, Applied Thermal Engineering, 109 (2016) 958-969.

[33] D. Hirsch, A. Steinfeld, Solar hydrogen production by thermal decomposition of natural gas using a vortex-flow reactor, Int. J. Hydrogen Energ., 29 (2004) 47-55.

[34] S. Rodat, S. Abanades, G. Flamant, Methane decarbonization in indirect heating solar reactors of 20 and 50 kW for a CO2-free production of hydrogen and carbon black, Journal of Solar Energy Engineering, Transactions of the ASME, 133 (2011).

[35] S. Rodat, S. Abanades, J.L. Sans, G. Flamant, A pilot-scale solar reactor for the production of hydrogen and carbon black from methane splitting, Int. J. Hydrogen Energ., 35 (2010) 7748-7758.

[36] E.E. Koepf, S.G. Advani, A.K. Prasad, A novel beam-down, gravity fed, solar thermochemical receiver/reactor for direct solid particle decomposition: Design, modeling, and experimentation, Int. J. Hydrogen Energ., 37 (2012) 16871-16887.

[37] S. Moller, R. Palumbo, The development of a solar chemical reactor for the direct thermal dissociation of zinc oxide, TRANSACTIONS-AMERICAN SOCIETY OF MECHANICAL ENGINEERS JOURNAL OF SOLAR ENERGY ENGINEERING, 123 (2001) 83-90.

[38] E.E. Koepf, S.G. Advani, A.K. Prasad, A. Steinfeld, Experimental Investigation of the Carbothermal Reduction of ZnO Using a Beam-Down, Gravity-Fed Solar Reactor, Industrial & Engineering Chemistry Research, 54 (2015) 8319-8332.

[39] A. Singh, J. Lapp, J. Grobbel, S. Brendelberger, J.P. Reinhold, L. Olivera, I. Ermanoski, N.P. Siegel, A. McDaniel, M. Roeb, C. Sattler, Design of a pilot scale directly irradiated, high temperature, and low pressure moving particle cavity chamber for metal oxide reduction, Solar Energy, 157 (2017) 365-376.

[40] A.C. Mejía, S. Afflerbach, M. Linder, M. Schmidt, Experimental analysis of encapsulated $CaO/Ca(OH)_2$ granules as thermochemical storage in a novel moving bed reactor, Applied Thermal Engineering, (2020) 114961.

[41] A.J. Schrader, G. De Dominicis, G.L. Schieber, P.G. Loutzenhiser, Solar electricity via an Air Brayton cycle with an integrated two-step thermochemical cycle for heat storage based

on Co_3O_4/CoO redox reactions III: Solar thermochemical reactor design and modeling, Solar Energy, 150 (2017) 584-595.

[42] G. Xiao, K. Guo, M. Ni, Z. Luo, K. Cen, Optical and thermal performance of a high-temperature spiral solar particle receiver, Solar Energy, 109 (2014) 200-213.

[43] P. Hallberg, M. Hanning, M. Rydén, T. Mattisson, A. Lyngfelt, Investigation of a calcium manganite as oxygen carrier during 99h of operation of chemical-looping combustion in a 10kWth reactor unit, International Journal of Greenhouse Gas Control, 53 (2016) 222-229.

[44] E.E. Koepf, S.G. Advani, A.K. Prasad, Experimental investigation of ZnO powder flow and feeding characterization for a solar thermochemical reactor, Powder Technology, 261 (2014) 219-231.

[45] M. Welte, R. Barhoumi, A. Zbinden, J.R. Scheffe, A. Steinfeld, Experimental Demonstration of the Thermochemical Reduction of Ceria in a Solar Aerosol Reactor, Industrial & Engineering Chemistry Research, 55 (2016) 10618-10625.

[46] A.C. Iniesta, M. Diago, T. Delclos, Q. Falcoz, T. Shamim, N. Calvet, Gravity-fed Combined Solar Receiver/Storage System Using Sand Particles as Heat Collector, Heat Transfer and Thermal Energy Storage Media, Energy Procedia, 69 (2015) 802-811.

[47] R.C. Knott, D.L. Sadowski, S.M. Jeter, S.I. Abdel-Khalik, H.A. Al-Ansary, A. El-Leathy, High Temperature Durability of Solid Particles for Use in Particle Heating Concentrator Solar Power Systems, in: ASME 2014 8th International Conference on Energy Sustainability collocated with the ASME 2014 12th International Conference on Fuel Cell Science, Engineering and Technology, Vol. Volume 1: Combined Energy Cycles, CHP, CCHP, and Smart Grids; Concentrating Solar Power, Solar Thermochemistry and Thermal Energy Storage; Geothermal, Ocean, and Emerging Energy Technologies; Hydrogen Energy Technologies; Low/Zero Emission Power Plants and Carbon Sequestration; Photovoltaics; Wind Energy Systems and Technologies, 2014.

[48] T. Tan, Y. Chen, Review of study on solid particle solar receivers, Renewable and Sustainable Energy Reviews, 14 (2010) 265-276.

[49] W. Pietsch, Understanding Agglomeration, Chemical Engineering Progress, 103 (2007).

[50] W. Pietsch, An interdisciplinary approach to size enlargement by agglomeration, Powder Technology, 130 (2003) 8-13.

[51] R. Gill, E. Bush, P. Haueter, P. Loutzenhiser, Characterization of a 6 kW high-flux solar simulator with an array of xenon arc lamps capable of concentrations of nearly 5000 suns, Rev. Sci. Instrum., 86 (2015) 125107.

[52] J. Hruby, Technical feasibility study of a solid particle solar central receiver for high temperature applications, in, Sandia National Labs., Livermore, CA (USA), 1986.

[53] T. Nguyen, C. Brennen, R. Sabersky, Funnel flow in hoppers, Journal of Applied Mechanics, 47 (1980) 729-735.

[54] E. Maynard, Ten steps to an effective bin design, CEP, American Society of Chemical Engineers: Tyngsboro, MA, USA, (2013) 25-32.

[55] N. Al-Din, D.J. Gunn, Metering of solids by a rotary valve feeder, Powder Technology, 36 (1983) 25-31.

[56] W.A. Beverloo, H.A. Leniger, J. van de Velde, The flow of granular solids through orifices, Chemical Engineering Science, 15 (1961) 260-269.

[57] I. Temizer, T.I. Zohdi, Agglomeration and refragmentation in microscale granular flows, International Journal of Fracture, 131 (2005) L37-L44.

[58] T.I. Zohdi, A computational framework for agglomeration in thermochecmially reacting granular flows, Proc. R. Soc. Lond. A., (2004).

[59] P. Hallberg, D. Jing, M. Rydén, T. Mattisson, A. Lyngfelt, Chemical Looping Combustion and Chemical Looping with Oxygen Uncoupling Experiments in a Batch Reactor Using Spray-Dried $CaMn_{1-x}M_xO_{3-\delta}$ (M = Ti, Fe, Mg) Particles as Oxygen Carriers, Energy & Fuels, 27 (2013) 1473-1481.

[60] H.E. Bush, R. Datta, P.G. Loutzenhiser, Aluminum-doped strontium ferrites for a two-step solar thermochemical air separation cycle: Thermodynamic characterization and cycle analysis, Solar Energy, 188 (2019) 775-786.

[61] D. de Ligny, P. Richet, High-temperature heat capacity and thermal expansion of SrTiO 3 and $SrZrO_3$ perovskites, Physical Review B, 53 (1996) 3013.

[62] S.M. Babiniec, E.N. Coker, A. Ambrosini, J.E. Miller, ABO_3 (A= La, Ba, Sr, K; B= Co, Mn, Fe) perovskites for thermochemical energy storage, in: AIP Conference Proceedings, Vol. 1734, AIP Publishing, 2016, pp. 050006.

[63] A.P. Muroyama, I. Guscetti, G.L. Schieber, S. Haussener, P.G. Loutzenhiser, Design and demonstration of a prototype 1.5kWth hybrid solar/autothermal steam gasifier, Fuel, 211 (2018) 331-340.

[64] Y. Forterre, O. Pouliquen, Flows of Dense Granular Media, 40 (2008) 1-24.